Regular Article

PHYSICAL CHEMISTRY RESEARCH
Published by the
Iranian Chemical Society
www.physchemres.org
info@physchemres.org

Phys. Chem. Res., Vol. 13, No. 4, 701-720, December 2025
DOI: 10.22036/pcr.2025.529463.2695

Spectral Measurements of a Novel Charge Transfer Complex Formed by a Heterocyclic Aromatic Amine and 1,4-Dinitrobenzene: A Combined Experimental and DFT Approach

N. Azizi-Balabeigloo, V. Hadigheh-Rezvan*, Gh. Ebrahimzadeh-Rajaei* and A. Shamel

Department of Chemistry, Ard.C., Islamic Azad University, Ardabil, Iran

(Received 9 June 2025, Accepted 2 August 2025)

A new hydrogen-bonded charge transfer complex (HB-CTC) was synthesized using melamine (MA) as the electron donor and 1,4-dinitrobenzene (*p*-DNB) as the π-acceptor in a 1:1 ratio. Both experimental and computational techniques fully characterized this complex. The orange solid complex formed by refluxing in methanol displayed clear spectroscopic characteristics. The FTIR analysis confirmed the hydrogen bond (N–H···O$^-$), indicated by red-shifted NH_2 and NO_2 vibrations. At the same time, NMR spectra showed distinct proton environments, confirming the structure of the complex. UV-Vis studies revealed a new charge transfer (CT) absorption band at 266 nm, which was not observed in the individual components. Density functional theory (DFT) calculations at the B3LYP/6-311G(d,p) level clarified the electronic structure, with the HOMO located on MA and the LUMO on *p*-DNB, revealing an energy gap of 3.113 *eV*. Thermodynamic data (ΔG° = -4.54 kcal mol^{-1}) and Mulliken/NBO analyses indicated that the formation is spontaneous and involves an efficient charge transfer (0.014 *e* from MA to *p*-DNB). This complex showed improved nonlinear optical properties, with its first- and second-order polarizabilities surpassing those of urea, pointing to potential optoelectronic applications. RDG and MEP analyses underscored the importance of stabilizing non-covalent interactions. This study offers a solid experimental and theoretical basis for developing CTCs with specific capabilities for materials science and organic electronics.

Keywords: Density functional theory, Electron donor-acceptor, Complex, Melamine, Dinitrobenzene

INTRODUCTION

Charge transfer complexes (CTCs) represent a fascinating intersection of chemistry and materials science, playing a pivotal role in various fields ranging from organic electronics to solar energy conversion [1]. When an electron is moved from a donor (D) molecule to an acceptor (A) molecule, these complexes are formed, resulting in a transitory state with unique optical and electrical characteristics [2]. This distinctive electron arrangement enables CTCs to exhibit remarkable behaviour, such as enhanced conductivity, altered light absorption, and the potential for applicative advancements in photochemical sensors, photonic devices, organic light-emitting diodes, and photovoltaic systems [3]. The synthesis of CTCs can be approached through several strategies, including combining small organic molecules, metal-organic frameworks, and conjugated polymers [4]. The electrical characteristics and stability of the final CTC are greatly influenced by the selection of donor and acceptor (D-A) materials. Advanced synthetic techniques, such as thermal evaporation, solution processing, and chemical vapor deposition, have created efficient interfaces for charge transfer [5]. Furthermore, developing new synthetic methods, such as click chemistry and self-assembly, has expanded the toolbox for constructing robust CT complexes with desirable electronic characteristics [6]. Recent advancements in synthetic methodologies have also allowed for the precise control of molecular architectures and the tuning of electronic properties through functionalization. Incorporating different substituents into

*Corresponding author. E-mail: gh_rajaei@iau.ac.ir

donor or acceptor moieties can significantly affect the efficiency of charge transfer (CT) processes by altering orbital overlaps and energy levels, enhancing the stability and performance of the resulting materials [7]. Integrating computational modeling alongside experimental synthesis provides further insight into the design and optimization of CTCs, enabling the prediction of electronic interactions and guiding the synthesis of novel materials [8].

The study of CTCs has gained momentum in recent years, driven by the quest for innovative solutions to energy challenges and the demand for efficient electronic materials [9]. Understanding the mechanisms that govern the formation and stability of these complexes is essential for designing novel materials with tailored properties [10]. Furthermore, their role in biological systems, particularly in electron transfer mechanisms in photosynthesis, enzyme function, biological energy conversion, the interaction of biomolecules, and electron transport in cellular respiration, highlights their significance beyond synthetic applications [11].

Hydrogen-Bonded Charge Transfer Complexes (HB-CTC) involve a charge transfer (CT) between a donor and an acceptor, specifically including hydrogen bonding as a significant stabilizing interaction [12]. The formation of hydrogen bonds between the involved molecules contributes to the stability and structure of the complex. In addition to the orbital overlap, hydrogen bonds provide additional stabilization. This interplay can affect the geometry and electronic properties of the complex, often leading to unique spectroscopic signatures [13]. These complexes are characterized by well-defined hydrogen-bonding networks, which can significantly influence their three-dimensional arrangement and intermolecular interactions. These are frequently researched for applications that leverage CT and specific molecular recognition processes, such as sensors, drug delivery systems, and organic photovoltaics. In essence, while all the complexes involve CT between donor and acceptor species, HB-CTCs are distinguished by the presence and role of hydrogen bonding [14].

Melamine (MA), an organic compound widely recognized for its use in producing plastics, resins, and fertilizers, has gained increasing attention in scientific research due to its remarkable ability to form CTCs with various electron acceptors [15]. These complexes are significant for their unique electronic properties and potential applications in sensing, organic photovoltaics, catalysis, and nanotechnology. CTCs involving MA exhibit fascinating spectroscopic behaviors, enabling the development of sensitive analytical techniques that detect pollutants and biomolecules at low concentrations. The conformational flexibility of MA and its interaction with various electron acceptors have been extensively studied, revealing insights into the mechanisms of CT and the effects of solvent polarity on complex stability [16].

1,4-Dinitrobenzene (*p*-DNB, *p*-dinitrobenzene) is a versatile organic molecule known for its applications in various fields, including organic synthesis, dye manufacturing, and as an industrial chemical. Its distinctive electronic structure, characterized by a strong electron-withdrawing nitro group, makes *p*-DNB an excellent candidate for forming CTCs with various electron donors [17]. These CTCs have garnered significant interest due to their unique photophysical properties, including altered absorption spectra and enhanced reactivity. These can be leveraged in fields such as sensing technologies and environmental chemistry. The formation of CTCs between *p*-DNB and different electron donors, such as aromatic amines and heterocyclic compounds, has been widely studied, revealing insights into the nature of electron donation and these complexes' stabilization through intermolecular interactions [18]. CTCs research has attracted much attention because of their distinct electrical characteristics, which differ greatly from those of their isolated components [19].

Computational studies have emerged as invaluable tools in the analysis of CTCs, providing insights into their electronic structure, stability, and dynamic behavior. Through density functional theory (DFT) and other computational methods, researchers can explore the nature of CT interactions at a molecular level, investigate the influence of solvent environments, and predict the optical properties of these complexes [20]. The capability to model CTCs computationally enables the exploration of a wide array of parameters, such as D-A characteristics, steric effects, and the influence of substituents, thus aiding in new materials design with customized electronic properties [21]. Recent advancements in computational techniques and algorithms have deepened our understanding of CTCs. Machine learning

approaches, for example, are being integrated with traditional computational methods to expedite the discovery process of CTCs with desired attributes [22].

The synthesis of novel compounds and their subsequent characterization is fundamental to advancing materials science, organic chemistry, and pharmacology [23]. In recent years, integrating spectroscopic techniques and computational methods, particularly DFT, has revolutionized our understanding of molecular structures and properties. Spectroscopic techniques, including mass spectrometry, NMR, IR, and UV-Vis, provide valuable insights into interactions and synthetic molecules' chemical environments. Concurrently, DFT presents a solid theoretical framework for predicting molecular behavior and electronic properties.

Numerous studies on heteroaromatics, including their CTCs, have recently been published in the literature [24-28]. For this reason, this study aims to synthesize and comprehensively characterize a novel hydrogen-bonded charge transfer complex (HB-CTC) formed between melamine (MA) as the electron/proton donor and 1,4-dinitrobenzene (*p*-DNB) as the π-acceptor. Utilizing a synergistic experimental and computational approach, we seek to: (i) Elucidate the structural and electronic properties of the [MA(*p*−DNB)] complex through spectroscopic techniques (FTIR, NMR, UV-Vis) and elemental analysis; (ii) Quantify charge transfer dynamics, thermodynamic stability, and frontier orbital interactions via density functional theory (DFT) calculations at the B3LYP/6-311G(d,p) level [29]; (iii) Evaluate the complex's nonlinear optical (NLO) response and potential for optoelectronic applications. This work establishes a foundational framework for designing functional HB-CTCs with tailored properties for advanced materials science.

Experimental Method

Merck provided pure melamine (MA) and 1,4-dinitrobenzene (*p*-DNB), which were utilized without additional purification. A high analytical grade of methanol was employed as the solvent. A Stuart SMP-3 device was used to measure the melting point. FTIR Perkin Elmer RXI was used to calculate the product infrared spectrum. Using DMSO-d_6 as the solvent, ^{1}H and ^{13}C NMR spectra were recorded on a Bruker 400 MHz instrument (400 MHz for ^{1}H and 100 MHz for ^{13}C). Chemical shifts are expressed in ppm (δ) relative to internal TMS, while coupling constants (J) are expressed in Hz. A quartz cell with a path length of 1.0 cm was placed inside a Shimadzu UV-1650PC spectrophotometer, which was used to record the UV-Visible absorption spectrum in the 100-800 nm range. Using a Perkin-Elmer CHN 2400 Series II (USA), elemental analysis of the carbon, hydrogen, and nitrogen atoms was conducted.

Synthesis of [MA(p-DNB)] Complex

A 1:1 stoichiometric ratio of MA to *p*-DNB was used to form the solid charge transfer complex ([MA(p-DNB)]). In synthesizing this complex, MA (0.1 mmol, 12.6 mg) was first dissolved in 50 ml of methanol solvent. To produce an even mixture, *p*-DNB (0.1 mmol, 16.8 mg) was dissolved in 10 ml of methanol and added to the initial solution. Then, gentle reflux was carried out at a temperature of 70 degrees Celsius for 6 h. After cooling the solution to room temperature, an orange-suspended solid was produced. Filtration was used to collect the suspended material, which was then vacuum-dried over anhydrous $CaCl_2$ after being washed four times with 40 ml of hot water. As seen in Fig. 1, an orange precipitate occurs when the *p*-DNB molecule is introduced to the MA dissolved in a heated methanol solvent. The spectral data of [MA(p-DNB)] complex are as follows:

Orange powder, yield 80%, 0.23 *g*; m.p. 175-177 ºC. FTIR (KBr) cm^{-1}: 3368 (NH_2), 1632 (C=C), 1558 and 1345 (NO_2), 1478 (C=C), 1409 (C=N), 1242 (C-N), and 1106 (N-H…O). ^{1}H NMR (400 MHz, DMSO-d_6): δ = 6.96 (s, 1H, NH), 6.98 (s, 4H, NH_2), 8.47 (d, 2H, $^3J_{HH}$ = 8 Hz, CH), 8.63 (d, 2H, $^3J_{HH}$ = 8 Hz, CH). ^{13}C NMR (100 MHz, DMSO-d_6): δ = 123.05 (CH), 125.64 (CH), 151.32 (C_{ipso}), 167.12 (C_{ipso}), 170.04 (C=N). Anal. Calc. for $C_9H_{10}N_8O_4$ (294.23): C, 36.74; H, 3.43; N, 38.08%. Found: C, 37.46; H, 3.57; N, 37.02%.

Computational Analysis

All of the examined molecules were created using the GaussView6 software. Next, *p*-DNB, MA, and their HB-CTC were computed using the Gaussian 09 program [30]. A theoretical analysis was conducted using the B3LYP function and the 6-311G(d,p) basis set within the DFT level of theory [31]. The use of several quantum mechanical techniques and basis sets for vibrational research has gained sufficient experience over the years.

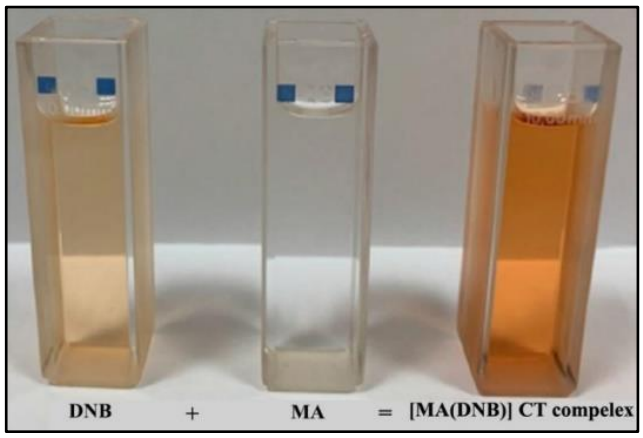

Fig. 1. View of colored solutions of MA, *p*-DNB, and [MA(*p*-DNB)] complex.

Everyone seems to agree that DFT, specifically the B3LYP method, which combines the Lee, Young, and Parr (LYP) correlation functional [32] with the three-parameter exchange functional of Becke, produces results that are sufficiently good and consistent enough, even when employing the standard 6-311G basis set at moderate computational costs. Every optimized molecule was subjected to a vibrational analysis to ensure it possessed no imaginary frequencies and was at a minimum vibrational energy. The optimal geometrical structural characteristics of the HB-CTC were determined, including the bond lengths, bond angles, Mulliken atomic charges, frontier molecular orbital (FMO) surfaces, molecular electrostatic potential (MEP) maps, and reactivity parameters. Reduced density gradient analysis was visualized using Multiwfn 3.8 software tools [33], generating contour plots or surfaces that represent regions of significant electron density changes.

RESULTS AND DISCUSSION

This study focuses on the creation of a new hydrogen-bonded charge transfer complex (HB-CTC) formed from the interaction of melamine (MA), acting as an electron and proton donor, and 1,4-dinitrobenzene (*p*-DNB), which serves as an electron and proton acceptor, in a molar ratio of 1:1 in methanol solvent under reflux conditions (see Scheme 1). The mechanism proceeds via a concerted three-step pathway involving solvent-mediated proton exchange, directional hydrogen bonding, and charge delocalization. In refluxing methanol (70 °C), MA and *p*-DNB undergo solvent-facilitated dissolution. Methanol acts as a proton-exchange mediator, enhancing the electrophilicity of *p*-DNB's nitro groups ($O^{\delta-}$) and the nucleophilicity of MA's amino/imino groups ($N^{\delta-}$–$H^{\delta+}$). The electron-rich amino group of MA (*e.g.*, –NH_2 or ring N) approaches the oxygen of a nitro group in *p*-DNB, forming an initial N–H···O hydrogen bond. Notably, the physical characteristics of the forming [MA(*p*-DNB)] complex differ from those of the component structures MA and *p*-DNB, including solubility and melting point. According to spectroscopic data, the two components are connected by a powerful H-bond (N-H….O^{-}) [34].

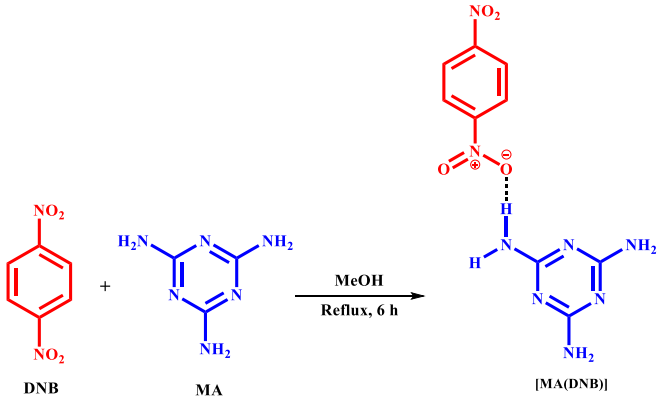

Scheme 1. Schematic method for preparing [MA(*p*-DNB)] complex

^{1}H NMR and ^{13}C NMR Spectral Study

The ^{1}H NMR and ^{13}C NMR spectral analyses are essential analytical techniques employed to investigate the structure of organic molecules. They used to examine the molecular environment of the protons in both MA and *p*-DNB within the HB-CTC. This can reveal information on the interaction of the two molecules, including changes in integration, splitting patterns, and chemical shifts.

The ^{1}H NMR spectrum of [MA(*p*-DNB)] complex is shown in Fig. 2. Melamine's principal amine group protons are revealed in this spectrum as discrete, singular signals at 6.96 ppm and 6.98 ppm. Furthermore, the two signals at 6.96 ppm and 6.98 ppm result from the different chemical environments of the NH_2 and NH protons in the triazine ring (MA). Meanwhile, the hydrogen atoms of the phenyl ring

show two doublet signals at 8.47 ppm and 8.63 ppm, which correspond to the 2,6- and 3,5- positions, respectively. The ^{1}H NMR spectrum reveals two clear, non-overlapping signals in the 8.47 ppm and 8.63 ppm regions, indicating that the protons of the phenyl ring in *p*-DNB exist in two different chemical environments. Thus, we can conclude that [MA(*p*-DNB)] complex has been successfully formed.

Figure 3 shows the [MA(*p*-DNB)] complex's ^{13}C NMR spectrum, where 5 signals are consistent with the suggested structure. The *ipso* carbon signals show up at 151.32 ppm and 167.12 ppm, whereas the chemical shifts for the *ortho* carbons are found at 123.05 ppm and 125.64 ppm. Furthermore, the C=N bond signal is seen at 170.04 ppm. The ingredient has been effectively produced and is a pure product because no other peaks are visible.

Gauge-independent atomic orbital (GIAO) methods are computational approaches used in quantum chemistry to account for the effects of magnetic fields on molecular systems [35]. The GIAO methodology is particularly useful for accurately predicting molecular properties sensitive to electronic structures, such as NMR chemical shifts, and for studying the electron transfer processes in CTCs. Usually, an electron is transferred in these complexes, which can cause substantial alterations in the electrical environment that affect the characteristics that NMR spectroscopy measures.

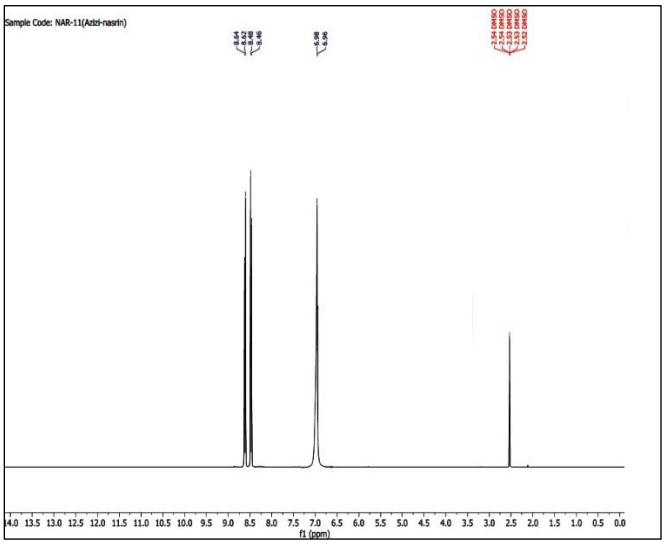

Fig. 2. ^{1}H NMR spectrum (DMSO-d_6, 400 MHz) of [MA(*p*-DNB)] complex.

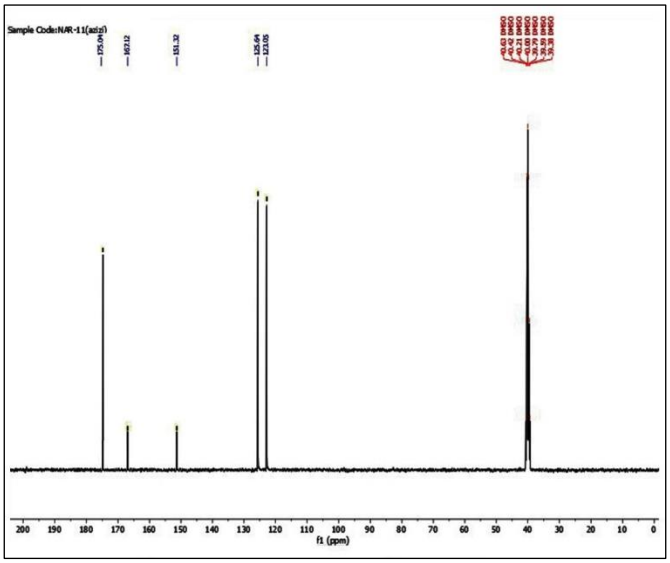

Fig. 3. ^{13}C NMR spectrum (DMSO-d_6, 100 MHz) of [MA(*p*-DNB)] complex.

Utilizing GIAO methods allows researchers to include the influence of a magnetic field on the electron distribution within these complexes, resulting in more accurate predictions of NMR shifts and other related properties.

Figures 4 and 5 show the calculated ^{1}H NMR and ^{13}C NMR spectra of [MA(*p*-DNB)] complex. Also, the [MA(*p*-DNB)] complex's estimated and experimental chemical shifts are listed and contrasted in Table 1. It is clear that computational chemical shifts are more accurate, and atoms with slight differences in an electronic environment are distinguished, such as the three carbon atoms of MA.

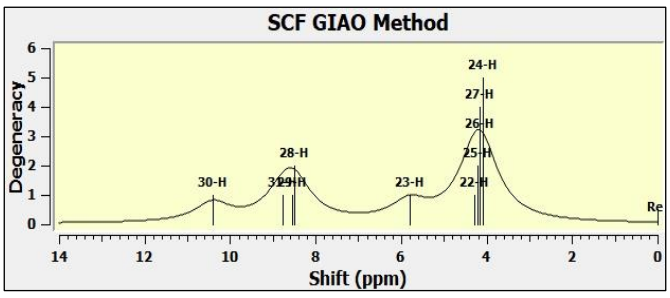

Fig. 4. Calculated ^{1}H NMR spectrum of [MA(*p*-DNB)] complex.

Table 1. The Calculated and Experimental Chemical Shifts of [MA(*p*-DNB)] Complex

Types of atoms	^{13}C NMR		Types of atoms	^{1}H NMR	
	Experimental δ (ppm)	Calculated		Experimental δ (ppm)	Calculated
C5-NH_2	170.04	172.39	NH (22, 25, 26, 27, 24)	6.96	4.18
C1-NH_2	170.04	170.17	NH (23)	6.98	5.80
C3-NH_2	170.04	169.69	CH (28, 29)	8.47	8.52
C16-NO_2	167.12	158.32	CH (31)	8.63	8.77
C19-NO_2	151.32	158.10	CH (30)	-	10.41
C20	123.05	130.17			
C21	125.64	133.15			
C18	123.05	128.45			
C17	125.64	129.13			

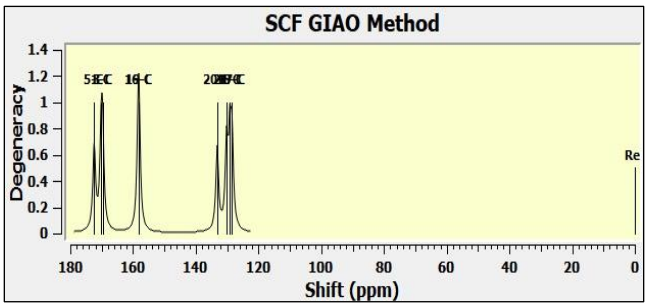

Fig. 5. Calculated ^{13}C NMR spectrum of [MA(*p*-DNB)] complex.

FTIR Spectroscopy

FTIR is a powerful analytical technique commonly used to study CTCs. Examining the characteristic absorption bands makes it possible to determine how these groups are involved in the CT process. Upon the formation of a CTC, modifications in the electronic environment of the D-A occur, which can be detected as shifts or changes in the intensity of IR absorption bands. For example, the interaction between the D-A may cause new peaks to emerge or existing peaks to change. The type and strength of the interactions inside the CTC can be evaluated using FTIR spectroscopy. The presence of specific bands indicative of CTC formation, such as the appearance of new peaks or the broadening of existing peaks, can provide insights into the strength of the interactions. The spectral features observed in FTIR can yield information about the degree of CT, the symmetry of the complex, and the overall molecular environment [36].

The frequency ranges of FTIR spectra, from 400 cm^{-1} to 4000 cm^{-1}, were used to record the absorption peaks of MA and *p*-DNB and the CTC experimentally, as illustrated in Fig. 6. The vibrational signal linked to the NH_2 group at 3368 cm^{-1} is visible in [(MA(*p*-DNB)] complex's FTIR spectrum. In MA complexes, NH_2 asymmetric stretching frequencies fall between 3500 cm^{-1} and 3300 cm^{-1}. The NH_2 symmetric vibration stretching peak in the current investigation is located at 3368 cm^{-1}; for melamine powder, this peak typically occurs at 3328 cm^{-1}. The N=O group-related symmetric and asymmetric stretching vibrations manifest at 1345 cm^{-1} and 1558 cm^{-1}, respectively. Furthermore, the C=N and C-N groups exhibit vibrations at 1409 cm^{-1} and 1242 cm^{-1}, respectively. An N-H…O group vibrational signal is detected at 1106 cm^{-1}. The asymmetric and symmetric stretching vibrations for the N=O group are located at 1552 cm^{-1} and 1358 cm^{-1}, respectively, in the *p*-DNB molecule's FTIR spectrum. The aromatic ring's C=C stretching bands manifest as pairs, with *p*-DNB displaying signals at 1638 cm^{-1} and 1436 cm^{-1}, and the complex displaying signals at 1632 cm^{-1} and 1478 cm^{-1}. Melamine's NH_2 group has stretching frequencies that range from

3300 cm^{-1} to 3500 cm^{-1}. The symmetric stretching vibration of NH_2 is seen in this work at 3368 cm^{-1}, while the corresponding vibration for crystalline MA is observed at 3334 cm^{-1} (see Fig. 6). Additionally, the experimental and calculated data for the IR spectra of [MA(*p*-DNB)] complex, which were determined using the B3LYP/6-311G(d,p) approach, are shown in Table 2.

When comparing the experimental IR spectrum with the calculated vibrational frequencies, we find that the results are remarkably similar. The computed vibrational frequencies were scaled; all wavenumbers were multiplied by 0.967. The computed values are quite similar when comparing the spectrum derived from the frequency calculations to the experimental infrared spectrum. The experimental results and the computed infrared frequencies agree quite well. A regression analysis yielded an $R^2 = 0.9953$ for the IR spectra data, as shown in Fig. 7. The complex's computational and experimental FTIR spectra are displayed in Fig. 8.

Table 2. Comparison of Calculated and Experimental IR Spectrum Data for the Complex

Experimental ν (in cm^{-1})	Calculated ν (in cm^{-1})	Vibration
3368	3220	ν(NH_2), stretching
1632	1626	ν(C=C), (in-ring) aromatic, stretching
1558	1595	$\nu_{as}(NO_2)$, stretching
1478	1479	ν(C=C), (in-ring) aromatic, stretching
1409	1389	ν(C=N), stretching
1345	1366	$\nu_s(NO_2)$, stretching
1242	1199	ν(C-N), bending
1106	1115	ν(N-H…O), bending
710	722	C-H out-of-plane bending

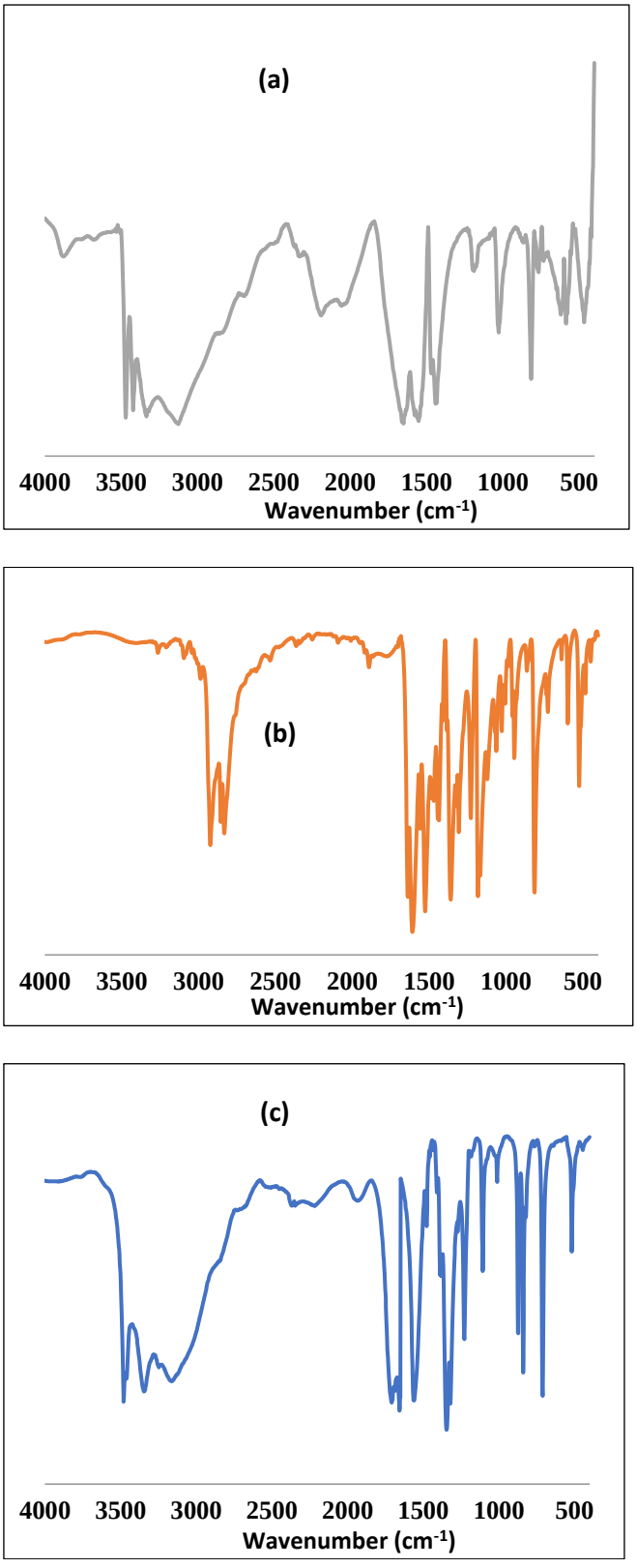

Fig. 6. Experimental FTIR spectra of (a) MA, (b) *p*-DNB, and (c) [MA(DNB)] complex.

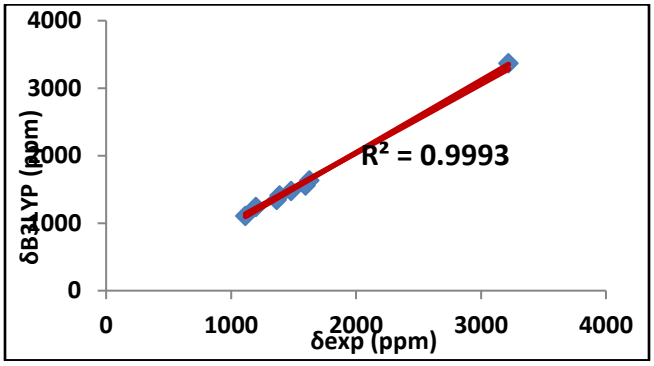

Fig. 7. Correlation diagram between experimental and calculated vibrational frequencies of [MA(*p*-DNB)] complex.

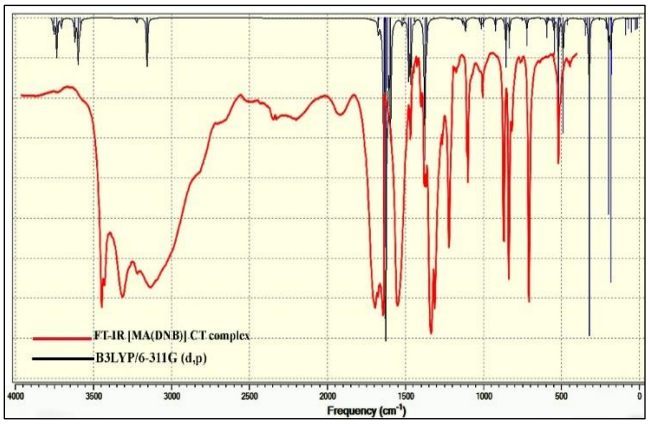

Fig. 8. Comparison of calculated and experimental IR spectra of [MA(*p*-DNB)] complex.

Elemental Analysis

CHN analysis (also known as elemental analysis for carbon, hydrogen, and nitrogen) is a useful technique in studying organic compounds. This analysis allows researchers to determine the elemental composition of a compound, which is crucial for understanding the structure and stoichiometry of the complex formed between D-A.

The elemental analysis for the [MA(*p*-DNB)] complex was performed, as presented in Table 3. The measured values from this analysis align closely with the calculated values, enabling us to confirm the molecular formula complex as $C_9H_{10}N_8O_4$.

UV-visible Absorption Spectra

UV-Vis spectroscopy of CTCs is a powerful analytical tool for studying the electronic transitions associated with these complexes. CT often leads to characteristic absorption bands in the UV-Vis spectrum. CTCs typically exhibit distinct absorption bands due to electronic transitions from the HOMO of the donor to the LUMO of the acceptor. The wavelength (λ_{max}) of the CT bands can be significantly red (bathochromic shift) or blue (hypsochromic shift) shifted compared to the absorption spectra of the pure components, indicating the interaction between the D and A. The CTC's creation can be confirmed by comparing its UV-Vis spectra to pure D and A. The spectra of the different components do not show the appearance of a new band. UV-Vis spectroscopy is commonly employed to confirm CTC formation and their stoichiometry. It allows researchers to study how different solvents or temperature conditions influence the formation and stability of CTCs.

CTCs can be engineered to respond to specific analytes through changes in their UV-Vis absorption, facilitating the development of sensing materials. Concerning earlier synthesis of the CTC, UV-Vis spectroscopy would be especially valuable for confirming the successful formation of the complex. You could analyze the spectrum to observe the formation of a new absorption band corresponding to the charge transfer. Measure the position and strength of the absorption band to understand the interactions between MA and *p*-DNB. UV-Vis absorption spectroscopy provides critical information about the electronic properties of charge transfer complexes.

Table 3. Integrated Elemental Analysis Data [MA(*p*-DNB)]

Molecular formula	Molecular weight ($g\ mol^{-1}$)	Calculated			Experimental		
		C	H	N	C	H	N
$C_9H_{10}N_8O_4$	294.23	36.74	3.43	38.08	37.46	3.57	37.02

Studying the complexes' formation, stability, and dynamics through spectrum analysis might be helpful for applications in materials science, sensor development, and basic chemical research [37].

This study examined the electronic absorption spectra of MA, *p*-DNB, and CTC within the wavelength range of 100-800 nm. The measurements were carried out at a concentration of 0.05 mM in a DMSO solvent. The complex's creation is indicated by the appearance of a new absorption band in the UV-Vis electronic absorption spectra at a wavelength of 266 nm. An electronic transition from the HOMO orbital (MA) to the LUMO orbital (*p*-DNB) is indicated by the 266 nm band in [MA(*p*-DNB)] complex. The electronic transitions of *p*-DNB and MA structures are associated with different absorption bands at wavelengths of 238 nm and 226 nm, respectively (see Fig. 9). Moreover, both products exhibit the same band at 266 nm. Some changes are seen, for the resulting product, this band is strongly intensified, and the other bands at higher energy are suppressed, which supports the charge transfer process. The calculated absorption spectrum of [MA(*p*-DNB)] complex shows a peak absorption band at 298 nm. The n → π* transition is responsible for the redshift of the complex (see Fig. 10). The MA, *p*-DNB, and the [MA(*p*-DNB)] complex's estimated and observed maximum absorption wavelengths (λ_{max}, nm) are shown in Table 4.

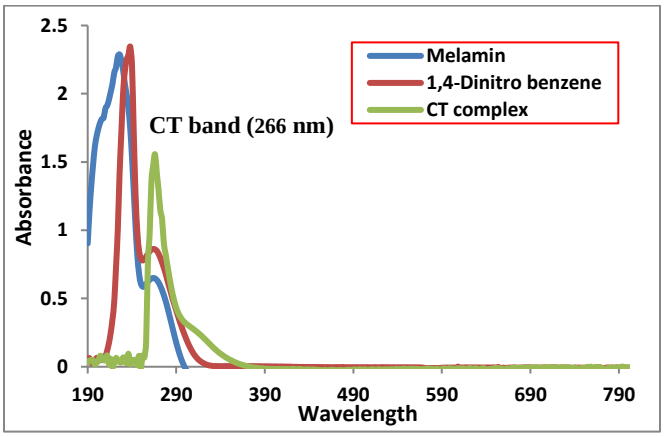

Fig. 9. Experimental UV-Vis spectra of MA, *p*-DNB, and [MA(*p*-DNB)] complex.

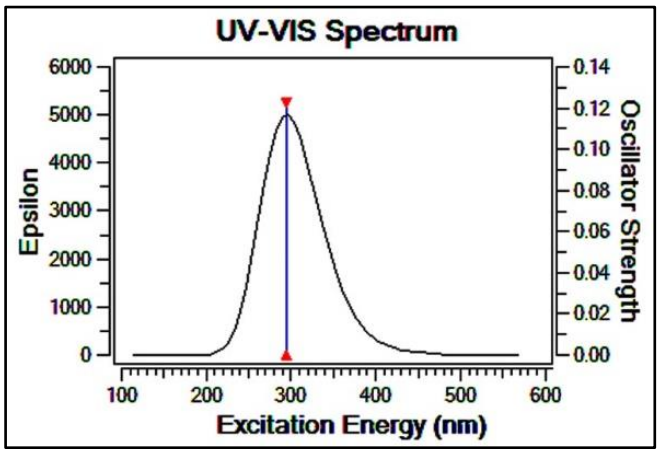

Fig. 10. Calculated UV-Vis spectrum of [MA(*p*-DNB)] complex.

Table 4. The Calculated and Experimental λ_{max} for MA, *p*-DNB, and [MA(*p*-DNB)] Complex

Compound	Calculated	Experimental
	λ_{max} (nm)	λ_{max} (nm)
MA	239	226
p-DNB	251	238
[MA(*p*-DNB)]	298	266

Optimized Geometries

Figure 11 displays the optimized molecular structures of the CTC as the free molecules MA and *p*-DNB in the gas phase. It also includes the atomic number system that was employed in this study. The ideal geometries of the D-A are parallelized, optimized once more, and allowed to relax freely. As a result, the two parts' orientation inside the CTC differs greatly from how they were originally set up before the optimization procedure. The potential vibrational spectrum for this structure shows all positive frequencies. It implies that the global energy minimum, or real equilibrium geometry, was determined for the structure. The complex formation between the D-A molecules as they approach one another is caused by intermolecular hydrogen bonding. As shown in Fig. 11, hydrogen bonds (H-bonds) are generally weak (with an O-H bond length of 1.691 Å); however, the number of potential H-bonds plays a crucial role in

stabilizing CTCs. In [MA(*p*-DNB)] complex, only one type of H-bond is present. This H-bond gives a notable vibrational effect. In the CTC, MA appears to approach *p*-DNB through the NH group.

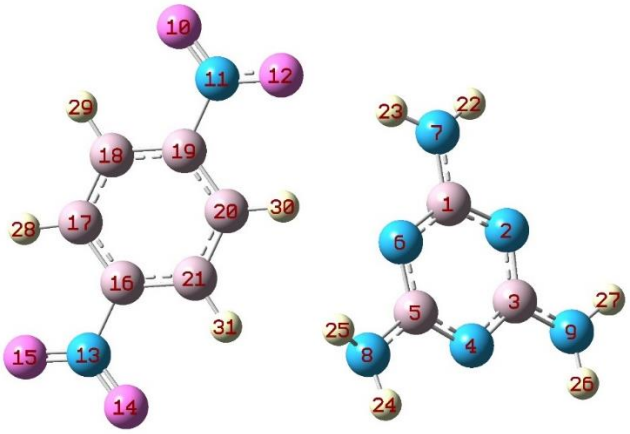

Fig. 11. Optimized geometric structure of [MA(*p*-DNB)] complex.

Only a small percentage of bond lengths stayed unchanged after the complex formed; the remainder changed. Some bonds were shortened, and some were extended. These results are consistent with the CT procedure, which has been shown in other research investigations [38]. In [MA(*p*-DNB)] complex, the bond length of the C1-N7 bond is 1.350 Å. The range of the bond length between *p*-DNB and MA molecules is 1.004-1.352 Å, while the range of [MA(*p*-DNB)] complex is 1.004-1.970 Å.

Comparable C–N experimental distances (1.398 Å) are noted for the melaminium ion. Every amino group and the ring are coplanar. The triazine ring and amino groups have C-N bonds ranging from 1.335 Å to 1.370 Å. While exterior N-C-N ring angles have 117 degrees, the triazine ring's C-N-C angles are comparable and equivalent to 114 degrees. The angles C, N, and H are about 118 degrees. Every H-N-H angle equals 120 degrees. Compared to MA, *p*-DNB molecules have a greater C–N spacing (1.27 Å). All 1,4-dinitrobenzene's C-C bond lengths are nearly similar, with values ranging from 1.350 to 1.352 Å. The 1.314-1.315 Å is the same for all N–O lengths [39].

The B3LYP/6-311G(d,p) approach was utilized to optimize the bond angles and bond lengths of the MA, *p*-DNB, and [MA(*p*-DNB)] complex in the DMSO Solvent. The results are shown in Tables 5 and 6. Only a small number of bonds were either stretched or shortened during complexation; there were no appreciable changes in bond lengths or bond angles for the D-A.

Table 5. Optimized Bond Length Values (Å) of MA, *p*-DNB, and [MA(*p*-DNB)] Complex in the Gas Phase

Bond length[a]	MA	DNB	[MA(*p*-DNB)]
C16-C17	-	1.350	1.391
C17-C18	-	1.350	1.387
C18-C19	-	1.352	1.392
C19-C20	-	1.350	1.390
C20-C21	-	1.351	1.391
C16-N13	-	1.270	1.486
C19-N11	-	1.271	1.484
N11-O10	-	1.314	1.220
N11-O12	-	1.315	1.225
N13-O14	-	1.314	1.221
N13-O15	-	1.315	1.222
C17H28	-	1.104	1.080
C18-H29	-	1.104	1.080
C20-H30	-	1.104	1.085
C21-H31	-	1.104	1.081
O12-H23	-	-	1.970
N7-H22	1.004	-	1.005
N7-H23	1.004	-	1.007
C1-N7	1.354	-	1.350
C1-N6	1.341	-	1.347
C1-N2	1.341	-	1.341
C5-N6	1.341	-	1.339
C5-N8	1.354	-	1.370
C5-N4	1.341	-	1.335
C3-N2	1.341	-	1.338
C3-N4	1.341	-	1.344
C3-N9	1.354	-	1.354
N8-H24	1.004	-	1.008
N8-H25	1.004	-	1.007
N9-H26	1.004	-	1.004
N9-H27	1.004	-	1.004

[a]For the numbering of atoms, refer to Fig. 11.

Table 6. Optimized Bond Angle values (degrees) of MA, *p*-DNB, and [MA(*p*-DNB)] Complex in the Gas Phase

Bond angle[a]	MA	*p*-DNB	[MA(*p*-DNB)]
C17-C16-C21	-	112.7	122.6
C16-C21-C20	-	123.8	118.9
C21-C20-C19	-	123.5	118.3
C20-C19-C18	-	112.6	122.9
C19-C18-C17	-	123.9	118.7
C18-C17-C16	-	123.5	118.6
C16-N13-O14	-	123.2	117.4
C16-N13-O15	-	122.9	117.3
C19-N11-O10	-	120.4	117.6
C19-N11-O12	-	124.6	117.8
C21-C16-N13	-	124.1	118.8
C17-C16-N13	-	123.2	118.5
C20-C19-N11	-	124.3	119.0
C18-C19-N11	-	123.1	118.1
O14-N13-O15	-	113.9	125.3
O10-N11-O12	-	115.0	124.6
N8-C5-N6	116.8	-	116.7
N8-C5-N4	116.8	-	116.8
N6-C5-N4	126.4	-	126.5
N6-C1-N2	126.4	-	125.6
N6-C1-N7	116.8	-	117.2
N7-C1-N2	116.8	-	117.2
C1-N2-C3	113.6	-	114.1
C5-N4-C3	113.6	-	113.6
N2-C3-N4	126.4	-	126.2
N2-C3-N9	116.8	-	117.1
N4-C3-N9	116.8	-	116.7
H24-N8-H25	121.3	-	116.8
H22-N7-H23	121.3	-	120.3
H26-N9-H27	121.3	-	120.5

[a]For the numbering of atoms, refer to Fig. 11.

Mulliken Electronic Charge

Mulliken electronic charge refers to the distribution of electronic charge in a molecule, commonly calculated using the Mulliken population analysis method from quantum chemistry. This method involves calculating the electronic wave function and permits the estimation of how the total electronic charge is distributed among the atoms in a CTC. In a charge transfer complex, where there is a significant movement of charge from one component to another, the Mulliken charge analysis helps to quantify the amount of charge that is localized on each entity in the complex. It can provide insights into the nature of the interaction between the D-A, helping chemists understand the stability and reactivity of the CTC. Mulliken charge values are often expressed in terms of atomic charge, which can be positive, negative, or neutral, reflecting the electron gain or loss at that particular atomic site as a result of the complex formation. These charges are indicative of the nature of the chemical bonding and the interaction between molecular entities. Overall, Mulliken analysis is a valuable tool when studying various systems in molecular science, including organic and inorganic chemistry, materials science, and biochemistry.

As illustrated in Table 7, the nitrogen atoms (from -0.414 e to -0.467 e) in the MA section and the oxygen atoms (from -0.250 e to -0.284 e), along with some carbon atoms from the *p*-DNB section, carry negative charges, making it easier for them to give up their electrons. The [MA(*p*-DNB)] complex's nitrogen and oxygen atoms are the active centers with the largest electron-donating capacity since they have the highest densities. These thick areas usually act as nucleophiles. On the other hand, some carbon atoms are classified as electron acceptors and electrophiles because they have positive charges. Therefore, significant evidence of reactivity features in these species is provided by the increase in Mulliken charges in certain atoms of electron acceptor molecules and the decrease in Mulliken charges in some atoms of electron donor molecules [40]. As seen in Table 7, in [MA(*p*-DNB)] complex, the Mulliken electronic charges of the O12 and H23 atoms are -0.284 e and 0.251 e, respectively.

Natural Bonding Orbital (NBO) Analysis

NBO analysis is a computational technique used in quantum chemistry to analyze and interpret the electron distribution and bonding properties of molecular systems. It's particularly useful for understanding complex systems such as CTCs. NBO analysis can provide insights into the nature of bonding interactions, the degree of CT between the D-A species, and the overall electronic structure of the complex.

Table 7. Mulliken Atomic Charges (e) on [MA(*p*-DNB)] Complex

Atom[a]	Charge	Atom[a]	Charge
O10	-0.250	C17	-0.054
O12	-0.284	C16	0.138
O14	-0.254	C5	0.434
O15	-0.258	C3	0.436
N11	0.189	C1	0.453
N13	0.177	H31	0.149
N9	-0.459	H30	0.186
N8	-0.459	H29	0.147
N7	-0.467	H28	0.147
N6	-0.450	H27	0.229
N4	-0.414	H26	0.229
N2	-0.416	H25	0.224
C21	-0.056	H24	0.225
C20	-0.054	H23	0.251
C19	0.113	H22	0.228
C18	-0.050		

[a]For the numbering of atoms, refer to Fig. 11.

NBO can indicate the presence of lone pairs, bonding pairs, and anti-bonding interactions. Analyze the second-order perturbation theory estimates to identify strong D-A interactions (key for charge transfer). Look for interactions between D-A electrons. Review the NBO populations and analyze the occupancy of bonding and anti-bonding orbitals. High occupancy in bonding NBOs and low occupancy in anti-bonding NBOs would suggest strong bonding, while significant population transfer implies substantial charge transfer. Assess Intermolecular Interactions: NBO analysis can help identify different types of interactions present in the CTC, such as π-π stacking and H-bonding.

Table 8 presents the calculated NBO atomic electronic charge of [MA(*p*-DNB)] complex by the B3LYP method. In this complex, the movement of electron density from MA to *p*-DNB has created a transient charge separation between the two species, which can be calculated by adding charges to each other. The sum is 0.014 e on the donor (MA) and -0.014 e on the acceptor (*p*-DNB). A positive charge on the donor and a corresponding negative charge on the acceptor indicate effective charge separation within the CTC, pointing toward the stability and strength of the interaction. This can be used to discuss the complex's pairing efficiency, ionicity, or donor-acceptor characteristics. These charges will generally be influenced by the intrinsic electronegativity of the D and A and the degree of CT. Mathematically, we can express the sum of NBO charges on the D-A as $Q_{total} = Q_{donor} + Q_{acceptor.}$ The total charge of [MA(*p*-DNB)] complex is zero, as the charges are assumed to be merely redistributing rather than creating or annihilating the charge.

Table 8. NBO Atomic Charges on [MA(*p*-DNB)] Complex

p-DNB		MA	
Atom[a]	Charge	Atom [a]	Charge
O10	-0.364	C5	0.649
O12	-0.405	C3	0.644
O14	-0.370	C1	0.649
O15	-0.374	H27	0.390
N11	0.523	H26	0.390
N13	0.515	H25	0.382
C17	-0.181	H24	0.387
C21	-0.180	H23	0.410
C20	-0.182	H22	0.389
C19	0.079	N9	-0.759
C18	-0.177	N8	-0.783
C16	0.085	N7	-0.761
H28	0.245	N6	-0.678
H29	0.244	N4	-0.649
H31	0.253	N2	-0.646
H30	0.275	Q (Donor)	0.014
Q (Acceptor)	-0.014		

[a]For the numbering of atoms, refer to Fig. 11.

Frontier Molecular Orbitals (FMOs)

FMOs are crucial in understanding CT complexes' electronic properties and reactivity. FMOs, specifically the highest occupied molecular orbital (HOMO) and the lowest unoccupied molecular orbital (LUMO), play a key role in CT

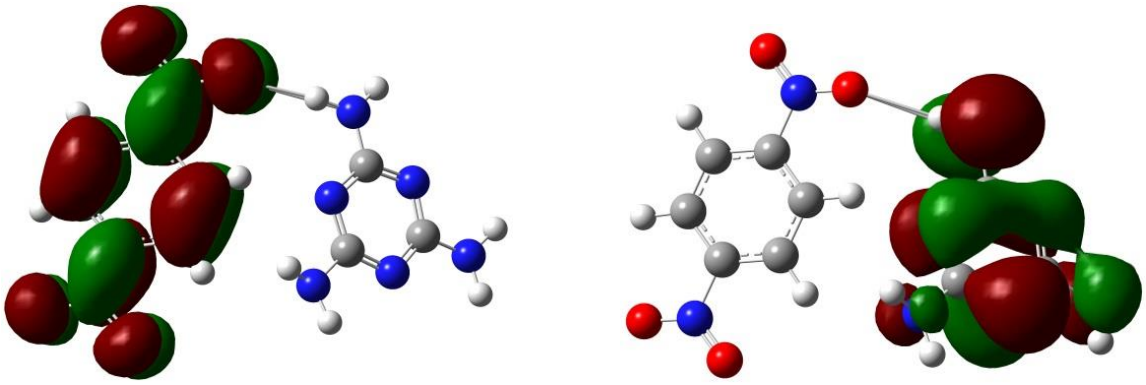

E_{LUMO} = -3.544 eV E_{HOMO} = -6.658 eV

Fig. 12. Frontier molecular orbital (FMO) model of [MA(*p*-DNB)] complex.

processes. Figure 12 illustrates that the HOMO orbital of [MA(*p*-DNB)] complex is concentrated primarily in the large region of MA. In contrast, the LUMO orbital is localized solely on *p*-DNB. This observation strongly suggests an effective CT process from the donor to the acceptor, forming a CTC. The energy gap (ΔE) between the frontier orbitals of this complex measures 3.113 eV. Interestingly, the HOMO orbital is typically found on the donor side, while the LUMO orbital is positioned on the acceptor side. This significant shift of the HOMO orbital towards the donor part and the LUMO orbital towards the acceptor part of the D-A complex facilitates the electron transfer process [41].

A direct indicator of a molecule's or complex's stability is the energy differential $\Delta(E_{LUMO}-E_{HOMO})$ between the energies of FMOs. A molecule or complex is more stable and resistant to light radiation if the absolute difference in values is larger. Our analysis confirms the stability of [MA(*p*-DNB)] complex by showing that its energy difference in DMSO is larger (3.113 eV) (See Fig. 12). This complex is characterized by a new set of energy levels different from the levels of various D-A molecules. The complex frequently exhibits unique optical and electrical features as a result of this energy level rearrangement, including strong coloration and the ability to absorb light in the visible spectrum.

We reported key parameters in Table 9 from quantum chemistry. Compound stability is indicated by a reduced energy gap between HOMO and LUMO [42]. A small electrical band gap value favors the soft character and high chemical reactivity. The HOMO is found at the MA moiety, and the LUMO is mostly found at the *p*-DNB moiety.

Table 9. Calculated Values of Quantum Chemical Parameters of [MA(*p*-DNB)] Complex

Quantum chemical parameters	Values (in eV)
E_{HOMO}	- 6.66
E_{LUMO}	- 3.54
$\Delta E = E_{LUMO} - E_{HOMO}$	3.11
$\eta = \Delta E/2$	1.56
$\sigma = 1/\eta$	0.64
$Pi = -(E_{HOMO} + E_{LUMO})/2$	5.10
$\chi = -Pi$	-5.10
$\Delta N_{max} = Pi/\Delta E$	1.64

Molecular Electrostatic Potential (MEP) Surface

The MEP surface is a valuable computational tool for visualizing the electrostatic potential distribution around a molecule. It provides insights into molecular properties such as reactivity, polarity, molecular recognition, charge distribution, and intermolecular interactions, which can be particularly important in CT complexes like [MA(*p*-DNB)]. MEP is defined as the electrostatic potential energy that a unit positive charge would experience at any point in space around the molecule. It is influenced by the distribution of atomic charges, electronegativity, and dipole moments within the molecule. The MEP is typically visualized on a three-dimensional surface, where regions of high electron density (negative potential) and low electron density (positive potential) are color-coded. Negative areas are often

depicted in red (high electron density), while positive potentials are shown in blue (low electron density).

Understanding which parts of the molecule are electrophilic (positively charged) or nucleophilic (negatively charged) can help predict how the CTC will react with other species. It provides insight into how the CTC might behave in various solvent environments or in the presence of other chemical species. It helps to understand binding sites for potential applications in sensors or pharmaceuticals, where the interactions are crucial for binding affinity. The MEP surface of [MA(*p*-DNB)] complex offers valuable insights into the electronic properties and potential reactivity of this system. By computing and visualizing the MEP, researchers can better understand how electronic interactions govern the behavior of the complex, paving the way for applications in materials science, organic electronics, and sensor development.

A CTC is generated from the electrostatic interaction of two pairs with opposite charges, one with high density and the other with low density [43]. The electrostatic potential surface of [MA(*p*-DNB)] complex is depicted in Fig. 13 with a deficiency of electron density (green shade) dispersed around the aromatic ring's C=C bonds. The existence of a high electron density, dispersed around the molecule's edges at the oxygen atoms, is indicated by the yellow color. This density may be implicated in the H-bond with the electron donor molecule, which will serve as the active site during the load transfer process. A CT cycle from the donor molecule to the π-system of the acceptor molecule is suggested by the change of positive to negative regions (green color) as the *p*-DNB molecule gets closer to the MA molecule. The pattern of electron densities corresponds to the charges found for each atom by Mulliken population analysis [44].

Non-Linear Optical (NLO) Property

The study of NLO properties of CTCs is important in materials science and photonics. CTCs with important NLO characteristics are utilized in optical switching, optical limiting, laser technology, and photonic devices. These characteristics are linked to a material's capacity to display a non-linear reaction to a given electric field, resulting in occurrences like second-harmonic generation (SHG), two-photon absorption, and electro-optic effects.

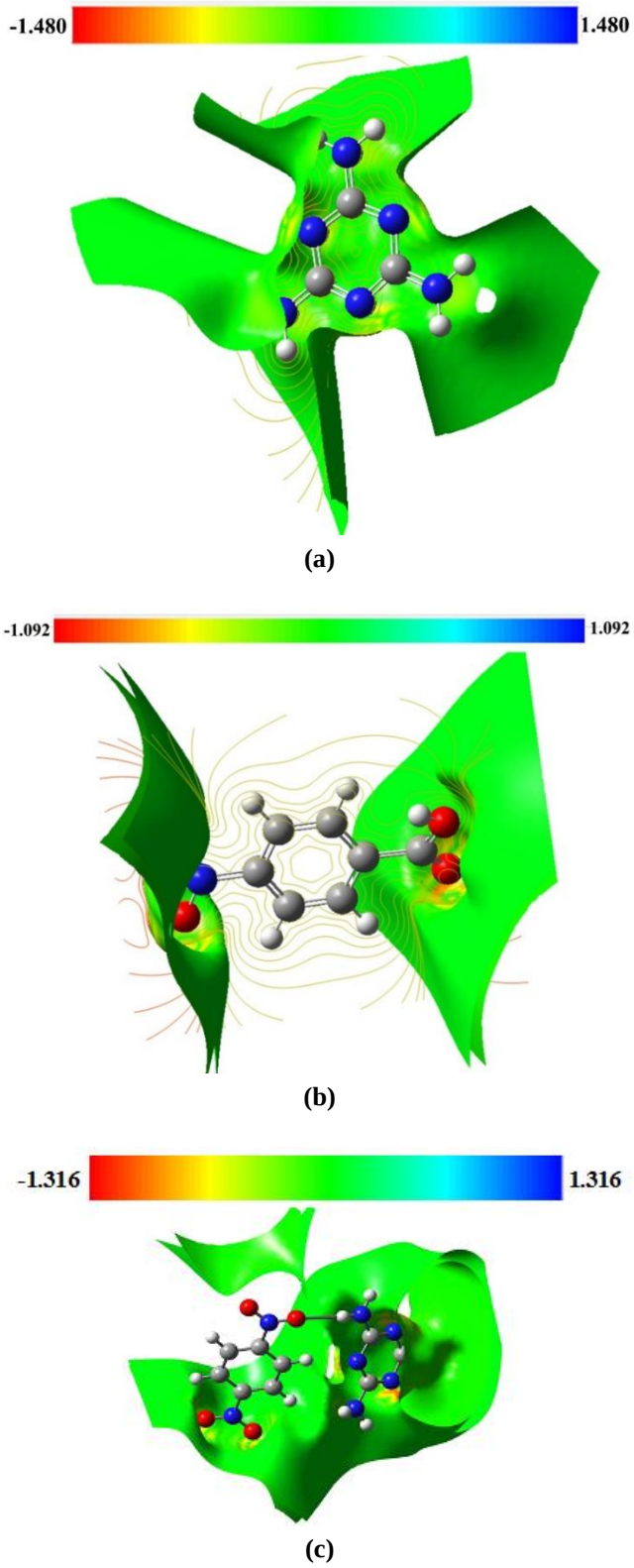

Fig. 13. Calculated MEPs for (a) MA, (b) *p*-DNB, and (c) [MA(*p*-DNB)] complex.

In CTCs, when exposed to light, CT takes place between the two entities. This CT can cause important changes in the electronic distribution, which is crucial for NLO responses. Different geometric layouts, distribution of electrons, and substituent types can improve nonlinear reactions. The measurement of NLO characteristics commonly involves assessing first-order polarizability (α) and second-order polarizability (β) [45]. The presence of the CT character enhances polarizability, making CT complexes suitable for improved NLO performance. The NLO characteristics are frequently heightened when the energy of the incident light aligns with the energy disparity of the electronic states engaged in the CT. Different experimental methods, such as Z-scan and SHG measurements, are employed to assess the NLO characteristics of CTCs, but they are difficult. So, computational techniques such as DFT can be used to forecast NLO characteristics and comprehend the molecular-level mechanisms [46].

We have computed the polarizabilities (α and β) using the "POLAR" keyword for the CTC and listed the data in Table 10 to analyze its nonlinear optical properties. The first-order polarizability (α) and second-order polarizability (β) are obtained from equations 1 and 2. The values of the first-order polarizability (25.226×10^{-24} esu) and second-order polarizability (4.289×10^{-30} esu) compared to those for urea (a standard NLO material) of 4.150×10^{-24} esu and 0.600×10^{-30} esu show that [MA(*p*-DNB)] complex could be a suitable candidate as an NLO material.

$$\alpha = \frac{1}{3}\,(\alpha_{xx} + \alpha_{yy} + \alpha_{zz}) \quad (1)$$

$$\beta = [(\beta_{xxx} + \beta_{xyy} + \beta_{xzz})^2 + (\beta_{yyy} + \beta_{yzz} + \beta_{yxx})^2 + (\beta_{zzz} + \beta_{zyy} + \beta_{zxx})^2]^{1/2} \quad (2)$$

The dipole moment (μ) is a three-dimensional vector representing the molecule's charge distribution. As a result, it can be used as a descriptor to describe how charge moves among molecules [47]. The positive and negative charge centers of the molecule determine the direction of the dipole moment vector within that molecule. [MA(*p*-DNB)] complex has a polarity of 1.76 D in the gas phase, which increases with the polarity of the medium.

Thermodynamic Parameters

The thermodynamic parameters of a CTC provide valuable insights into the stability, formation, and complex interactions under various conditions. The Gibbs free energy change (ΔG^o) indicates the spontaneity of the charge transfer process [48]. The enthalpy change (ΔH^o) reflects the heat absorbed or released during the formation of the CTC. The entropy change (ΔS^o) represents the change in disorder associated with the formation of the CTC [49]. This can be derived from the ΔG^o and ΔH^o using the Gibbs free energy equation ($T\Delta S^o = \Delta H^o - \Delta G^o$). Through careful computational analysis, we can obtain reliable values for ΔH^o, ΔG^o, and ΔS^o, contributing to a deeper understanding of the nature of CTCs. Understanding the thermodynamic

Table 10. Calculated Nonlinear Optical Properties for [MA(*p*-DNB)] Complex

μ (*D*) = 1.76	β_{yxx} = 192.956
first-order polarizability (α)	β_{xyy} = 104.578
α_{XX} = 210.998	β_{yyy} = -121.767
α_{XY} = -2.788	β_{zxx} = 28.739
α_{YY} = 208.602	β_{xyz} = -101.048
α_{XZ} = -7.634	β_{zyy} = 0.986
α_{YZ} = -7.751	β_{xzz} = -14.778
α_{ZZ} = 91.051	β_{yzz} = 45.906
α = 170.217 a.u.	β_{zzz} = 29.726
$\alpha = 25.226 \times 10^{-24}$ esu	β (a.*u.*) = 496.353
Second-order polarizability (β)	β (*esu*) = 4.289×10^{-30} $cm^5.esu^{-1}$ = esu
β_{xxx} = -568.466	

parameters of the complex is essential for elucidating its stability, reactivity, and interaction with other species [50].

Table 11 presents the calculated thermodynamic parameters for [MA(*p*-DNB)] complex using the B3LYP/6-311G(d,p) level of theory in the gas phase. The values of ΔH°, ΔG°, and ΔS° for the complex are -13.48 kcal mol^{-1}, -4.54 kcal mol^{-1}, and -0.03 kcal mol^{-1}, respectively (see Table 11). Strong interaction between the reactants is indicated by the negative values of ΔH° and ΔG°. Furthermore, as ΔS° rises, the complex becomes more disordered and stable. As a result, the findings of the thermodynamic parameters show that the complex formed spontaneously and that the molecule was capable of forming a stable complex. The complex formation is driven by the positive ΔS° and negative ΔH° signals.

Table 11. Thermodynamic Parameters of [MA(*p*-DNB)] Complex

ΔH° (kcal mol^{-1})	ΔG° (kcal mol^{-1})	ΔE° (kcal mol^{-1})	ΔS° (kcal K^{-1} mol^{-1})
-13.48	-4.54	-12.71	-0.03

Reduced Density Gradient (RDG) Analysis

Reduced density gradient analysis is an important computational chemistry tool used to investigate electron density properties in molecular systems, including CTCs. The RDG provides insights into the electronic structure, including regions of strong electron interaction, which can be particularly useful for understanding bonding, non-covalent interactions, and CT processes [50]. The RDG helps to normalize the density gradient by accounting for the local electron density. RDG analysis allows for the visualization of electron density variation across the CTC, helping to identify where electron donation and acceptance occur, which is used to assess interactions such as hydrogen bonds, π–π stacking, and ionic interactions, all of which play a significant role in the stabilization of CTCs. By examining the regions with significant RDG, researchers can identify how the charge is distributed upon excitation and the pathways available for CT. These maps highlight areas of electron richness and deficiency, enhancing our understanding of the behavior of the CTC [51].

Figure 14 displays the complex's gradient isosurface and scatter plot formed from MA and *p*-DNB. In the RDG scatter spectrum, λ2(r) varies from 0.000 a.u. to 2.00 a.u., classified into three colors: blue, green, and red. The presence of green flakes suggests the existence of weak non-covalent interactions. These subtle interactions can also be seen in RDG scatter plots varying from -0.02 a.u. to 0.035 a.u. Moreover, the O-H…π interactions are represented by the red-green mixed flaky region, which is found between 0.00 and 0.05 a.u. This interplay includes hydrogen atoms from MA and the π-electrons of *p*-DNB. The red spikes on the right side of the RDG scatter plot illustrate the repulsive interactions among the carbon atoms in the two components [52].

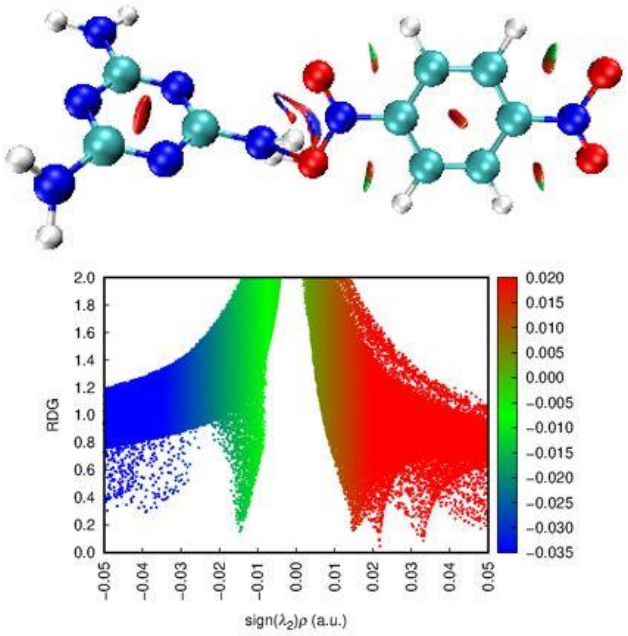

Fig. 14. Calculated reduced density gradient plot of [MA(*p*-DNB)] complex.

CONCLUSION

This study successfully synthesized and characterized a novel HB-CTC between MA and *p*-DNB, demonstrating its unique structural, electronic, and optical properties.

Spectroscopic techniques, including FTIR, NMR, and UV-Vis, confirmed the formation of the complex through distinct hydrogen bonding (N–H···O) interactions and a characteristic charge transfer absorption band at 266 nm. NMR spectra revealed differentiated proton environments (δ = 8.47-8.63 ppm for aromatic CH and δ = 6.96-6.98 ppm for NH/NH_2), corroborating the complex's structure. Density Functional Theory calculations at the B3LYP/6-311G(d,p) level of theory provided critical insights into the electronic structure, revealing HOMO localization on the donor (MA) and LUMO on the acceptor (*p*-DNB), with a narrowed energy gap (ΔE) of 3.113 eV that underscores enhanced charge transfer efficiency. Thermodynamic analyses ($\Delta G°$ = -4.54 kcal mol^{-1}, $\Delta H°$ = -13.48 kcal mol^{-1}) affirmed the spontaneity and stability of the complex, while Mulliken and NBO charge distributions quantified effective electron transfer (0.014 **e** from MA to *p*-DNB). Notably, the complex exhibited promising nonlinear optical (NLO) properties, with first- and second-order polarizabilities ($\alpha = 25.23 \times 10^{-24}$ esu, $\beta = 4.29 \times 10^{-30}$ esu) surpassing urea, positioning it as a candidate for optoelectronic applications. Reduced density gradient (RDG) and molecular electrostatic potential (MEP) analyses further elucidated the stabilizing non-covalent interactions governing the complex's architecture. These findings advance the understanding of HB-CTC and establish a robust experimental-computational framework for designing functional materials tailored for organic electronics, sensing, and photonic devices. Future studies could explore solvent effects, scalability, and device integration to harness the full potential of this complex in practical applications.

ACKNOWLEDGMENT

The authors are grateful to the Chemistry Department of Islamic Azad University, Ardabil Branch, for providing the materials and instrumental resources.

REFERENCES

[1] Baharfar, M.; Hillier, A. C.; Mao, G., Charge-Transfer Complexes: Fundamentals and Aadvances in Catalysis, Sensing, and Optoelectronic Applications. *Adv. Mater.* **2024**, *36*(42), 2406083, https://doi.org/10.1002/adma.202406083.

[2] Chen, X.; Zhang, X.; Xiao, X.; Wang, Z.; Zhao, J., Recent Developments on Understanding Charge Transfer in Molecular Electron Donor-Acceptor Systems. *Angew. Chem., Int. Ed.* **2023**, *62*(16), e202216010, https://doi.org/10.1002/anie.202216010.

[3] Wang, W.; Luo, L.; Sheng, P.; Zhang, J.; Zhang, Q., Multifunctional Features of Organic Charge-Transfer Complexes: Advances and Perspectives. *Chem–Eur. J.* **2021**, *27*(2), 464-490, https://doi.org/10.1002/chem.202002640.

[4] Liu, J.; Huang, J.; Zhang, L.; Lei, J., Multifunctional Metal–Organic Framework Heterostructures for Enhanced Cancer Therapy. *Chem. Soc. Rev.* **2021**, *50*(2), 1188-1218, https://doi.org/10.1039/D0CS00178C.

[5] Heydari Gharahcheshmeh, M.; Gleason, K. K., Device Fabrication Based on Oxidative Chemical Vapor Deposition (OCVD) Synthesis of Conducting Polymers and Related cConjugated Organic Materials. *Adv. Mater. Interfaces* **2019**, *6*(1), 1801564, https://doi.org/10.1002/admi.201801564.

[6] Wu, J.; Lin, J.; Huang, P., Harnessing Abiotic Organic Chemistry in Living Systems for Biomedical Applications. *Chem. Soc. Rev.* **2023**, *52*(12), 3973-3990, https://doi.org/10.1039/D3CS00280B.

[7] Shen, D.; Chen, W. C.; Lo, M. F.; Lee, C. S., Charge-Transfer Complexes and Their Applications in Optoelectronic Devices. *Mater. Today Energy* **2021**, *20*, 100644, https://doi.org/10.1016/j.mtener.2021.100644.

[8] Shahzad, K.; Mardare, A. I.; Hassel, A. W., Accelerating Materials Discovery: Combinatorial Synthesis, High-Throughput Characterization, and Computational Advances. *Sci. Technol. Adv. Mater.: Methods* **2024**, *4*(1), 2292486, https://doi.org/10.1080/27660400.2023.2292486.

[9] Batth, I. S.; Mitra, A.; Rood, S.; Kopetz, S.; Menter, D.; Li, S., CTC Analysis: an Update on Technological Progress. *Transl. Res.* **2019**, *212*, 14-25, https://doi.org/10.1016/j.trsl.2019.07.003.

[10] Gomes, B. S.; Simões, B.; Mendes, P. M., The Increasing Dynamic, Functional Complexity of Bio-Interface Materials. *Nat. Rev. Chem.* **2018**, *2*(3), 0120, https://doi.org/10.1038/s41570-018-0120.

[11] Zheng, T.; Li, J.; Ji, Y.; Zhang, W.; Fang, Y.; Xin, F.; Dong, W.; Wei, P.; Ma, J.; Jiang, M., Progress and Prospects of Bioelectrochemical Systems: Electron Transfer and Its Applications in the Microbial Metabolism. *Front. Bioeng. Biotechnol.* **2020**, *8*, 10, https://doi.org/10.3389/fbioe.2020.00010.

[12] Beigloo, N. A. B.; Rezvan, V. H.; Ebrahimzadeh-Rajaei G.; Shamel, A., New Charge Transfer Complex Between Melamine and 4-Nitrobenzoic Acid: Synthesis, Spectroscopic Characterization, and DFT Studies. *J. Mol. Struct.* **2025**, *1322* (2), 140469, https://doi.org/10.1016/j.molstruc.2024.140469.

[13] Samuel, H. S.; Nweke-Maraizu, U.; Etim, E. E., Understanding Intermolecular and Intramolecular Hydrogen Bonds: Spectroscopic and Computational Approaches. *J. Chem. Rev.* **2023**, *5*(4), 439-465, https://doi.org/10.48309/JCR.2023.407989.1235.

[14] Grabowski, S. J., What Is the Covalency of Hydrogen Bonding? *Chem. rev.* **2011**, *111*(4), 2597-2625, https://doi.org/10.1021/cr800346f.

[15] Wang, Y.; Chen, Z.; Lu, Y.; Yang, L.; Xu, T.; Wu, H.; Zhang, J.; He, L., A Review of Application, Modification, and Prospect of Melamine Foam. *Nanotechnol. Rev.* **2023**, *12*(1), 20230137, https://doi.org/10.1515/ntrev-2023-0137.

[16] Stsiapura, V. I.; Kurhuzenkau, S. A.; Kuzmitsky, V. A.; Bouganov, O. V.; Tikhomirov, S. A., Solvent Polarity Effect on Nonradiative Decay Rate of Thioflavin T. *J. Phys. Chem. A* **2016**, *120*(28), 5481-5496, https://doi.org/10.1021/acs.jpca.6b02577.

[17] Conde, R. S.; Torres Barroso, L.; Pérez Edighill, S. G.; Yerien, D. E.; Lantaño, B.; Baroncini, M.; Barata-Vallejo, S.; Postigo, A., Photocatalytic Perfluoroalkylation of Disulfides and Diselenides. Syntheses of Perfluoroalkyl Thio-and Seleno-ethers. *J. Org. Chem.* **2024**, *89*(15), 10867-10877, https://doi.org/10.1021/acs.joc.4c01149.

[18] Nemukhin, A. V.; Grigorenko, B. L.; Khriachtchev, L.; Tanskanen, H.; Pettersson, M.; Räsänen, M., Intermolecular Complexes of HXeOH with Water: Stabilization and Destabilization Effects. *J. Am. Chem. Soc.* **2002**, *124*(36), 10706-10711, https://doi.org/10.1021/ja0266870.

[19] Lin, M.; Chen, J. F.; Lu, Y. T.; Zhang, Y.; Song, J.; Hou, S.; Ke, Z.; Tseng, H. R., Nanostructure Embedded Microchips for Detection, Isolation, and Characterization of Circulating Tumor Cells. *Acc. Chem. res.* **2014**, *47*(10), 2941-2950, https://doi.org/10.1021/ar5001617.

[20] Golipour-Chobar, E.; Salimi, F.; Ebrahimzadeh Rajaei, G., Boron Nitride Nanocluster as A Carrier for Lomustine Anticancer Drug Delivery: DFT and Thermodynamics Studies. *Monatsh. fur Chem.* **2020**, *151*, 309-318, https://doi.org/10.1007/s00706-020-02564-y.

[21] Golipour-Chobar, E.; Salimi, F.; Ebrahimzadeh-Rajaei, G., Sensing of Lomustine Drug by Pure and Doped C48 Nanoclusters: DFT Calculations. *Chem. Methodol.* **2022**, *6*, 790-800, DOI: 10.22034/ CHEMM.2022.344895.1555.

[22] Rezvan, V. H., Vibrational Analysis, Frontier Orbitals, Optical and Structural Properties of 1,2-Dithiete and Di-Thiolene Derivatives: A Quantum Mechanical Study. *Results Chem.* **2024**, *7*, 101522, https://doi.org/10.1016/ j.rechem.2024.101522.

[23] Kamali, F.; Ebrahimzadeh Rajaei, G.; Mohajeri, S.; Shamel, A.; Khodadadi-Moghaddam, M., Adsorption Behavior of Metformin Drug on the C_{60} and C_{48} Nanoclusters: A Comparative DFT Study. *Monatsh. fur Chem.* **2020**, *151*, 711-720, https://doi.org/10.1007/ s00706-020-02597-3.

[24] Das, S.; Rawal, P.; Bhattacharjee, J.; Devadkar, A.; Pal K.; Gupta, P.; Panda, T. K., Indium Promoted C (sp^3)–P Bond Formation by the Domino A 3-Coupling Method–A Combined Experimental and Computational Study. *Inorg. Chem. Front.* **2021**, *8*(5), 1142-1153, https://doi.org/10.1039/D0QI01210F.

[25] Eremina, O. E.; Samodelova, M. V.; Ferree, M. V.; Shekhovtsova, T. N.; Veselova, I. A., Capturing Polycyclic Aromatic Sulfur Heterocycles in Electron Donor–Acceptor Complexes. *Mendeleev Commun.* **2021**, *31*(3), 326-329, https://doi.org/10.1016/ j.mencom.2021.04.015.

[26] Parvini, E.; Vatanparast, M.; Saedi, L., *Ab Initio* Studies on the Interplay Between Unconventional B••• X Halogen Bond and Lithium/Hydrogen/Halogen Bond in

HB $(CO)_2$••• XCN••• YF (X = Cl, Br; Y = Li, H, Cl) Complexes. *Phys. Chem. Res*. **2017**, *5*(4), 771-81, DOI: 10.22036/pcr.2017.90701.1394.

[27] Salehi, S.; Mashmoul Moghadam, S. M.; Tarin, M.; Shokooh Saljooghi, A., Pharmaceutical Nickel(II) Chelation Properties of 3-Hydroxyflaven, Deferiprone and Maltol Metal Chelators: A Density Functional Study. *Phys. Chem. Res*. **2020**, *8*(1), 91-110, DOI: 10.22036/pcr.2019.202156.1677.

[28] Behjatmanesh-Ardakani, R., DFT-PBE, DFT-D, and MP2 Studies on the H_2O••• HNH and HOH••• NH_2 Hydrogen Bonds in Water-Aniline Complexes. *Phys. Chem. Res*. **2016**, *4*(1), 95-107, DOI: 10.22036/pcr.2016.12401.

[29] Behmanesh, A.; Salimi, F.; Ebrahimzadeh Rajaei, G., Adsorption Behavior of Letrozole on Pure, Ge-and Si-Doped C_{60} Fullerenes: A Comparative DFT Study. *Monatsh. fur Chem.* **2020**, *151*, 25-32, https://doi.org/10.1007/s00706-019-02524-1.

[30] Caricato, M.; Frisch, M. J.; Hiscocks, J.; Frisch, M. J., Gaussian 09: IOps Reference: Gaussian Wallingford, CT, USA: 2009; p. 24-28.

[31] Karjabad, K. D.; Mohajeri, S.; Shamel, A.; Khodadadi-Moghaddam, M.; Rajaei, G. E., Boron Nitride Nanoclusters as A Sensor for Cyclosarin Nerve Agent: DFT and Thermodynamics Studies. *SN Appl. Sci.* **2020**, *2*(547), 1-8, https://doi.org/10.1007/s42452-020-2411-2.

[32] Xu, X.; Goddard III, W. A., The X3LYP Extended Density Functional for Accurate Descriptions of Nonbond Interactions, Spin States, and Thermochemical Properties. *Proc. Natl. Acad. Sci.* **2004**, *101*(9), 2673-2677, https://doi.org/10.1073/pnas.0308730100.

[33] Abhijith, R.; Parakkal, S. C.; Datta, R.; Alharbi, N. S.; Muthu, S., Quantum Computational, Solvation and In-Silico Biological Studies of a Potential Anti-Cancer Thiophene Derivative. *J. Mol. Liq.* **2024**, *405*, 125077, https://doi.org/10.1016/j.molliq.2024.125077.

[34] Song, H. X.; Han, Q. Y.; Zhao, C. L.; Zhang, C. P., Fluoroalkylation Reactions in Aqueous Media: A Review. *Green Chem.* **2018**, *20*(8), 1662-1731, https://doi.org/10.1039/C8GC00078F.

[35] Franzke, Y. J.; Yu, J. M., Quasi-Relativistic Calculation of EPR g Tensors With Derivatives of the Decoupling Transformation, Gauge-Including Atomic Orbitals, and Magnetic Balance. *J. Chem. Theory Comput.* **2022**, *18*(4), 2246-2266, https://doi.org/10.1021/acs.jctc.1c01175.

[36] Yan, J.; Lei, Z.; Li, Z.; Wang, Z.; Ren, S.; Kang, S.; Wang, X.; Shui, H., Molecular Structure Characterization of Low-Medium Rank Coals *via* XRD, Solid State ^{13}C NMR and FTIR Spectroscopy. *Fuel* **2020**, *268*, 117038, https://doi.org/10.1016/j.fuel.2020.117038.

[37] Mostafa, A.; Madrahimov, S.; Fadlallah, J.; AlQaradawi, S. Y., UV–Vis, IR Spectra, Mass Spectrometry and Thermal Studies of Charge Transfer Complexes Formed in the Reaction of 1,4,8,11-Tetraazacyclotetradecane with π-Electron Acceptors. *J. Mol. Liq.* **2019**, *284*, 616-624, https://doi.org/10.1016/j.molliq.2019.04.040.

[38] Fall, W. S.; Baschnagel, J. R.; Lhost, O.; Meyer, H., Role of Short Chain Branching in Crystalline Model Polyethylenes. *Macromolecules* **2022**, *55*(19), 8438-8450, https://doi.org/10.1021/acs.macromol.2c00938.

[39] Domasevitch, K. V.; Senchyk, G. A.; Krautscheid, H., High-Yielding Syntheses, Crystal Structures and Hirshfeld Surface Analysis of Bis-1,1′-(2-nitropropenes) Extended with Benzene-1, 4-diyl and Biphenyl-4, 4′-diyl Spacers. *J. Chem. Crystallogr.* **2025**, *55*, 22-34, https://doi.org/10.1007/s10870-024-01032-3.

[40] Hussein, H. A., A DFT Study of Structural-Stability, Mulliken Charges, MEP, FMO, and NLO Properties of Trans Aalkenyl Substituted Chalcones Conformers: Theoretical Study. *Struct. Chem.* **2023**, *34*(6), 2201-2223, https://doi.org/10.1007/s11224-023-02139-7.

[41] Rezaei-Sameti, M.; Rezaei, A., A Computational Assessment of the Interaction of 5Fluorouracil (5FU) Drug Connected to $B_{12}P_{12}$ and $ScB_{11}P_{12}$ Nanocages with Adenine Nucleobase: DFT, AIM, TD-DFT Study. *Struct. Chem.* **2024**, *35*(1), 105-118, https://doi.org/10.1007/s11224-023-02141-z.

[42] Kamali, F.; Ebrahimzadeh-Rajaei, G.; Mohajeri, S.; Shamel, A.; Khodadadi-Moghaddam, M., A Computational Design of $X_{24}Y_{24}$ (X = B, Al, and Y = N, P) Nanoclusters as Effective Drug Carriers for Metformin Anticancer Drug: A DFT Insight. *Inorg. Chem. Commun.* **2022**, *141*, 109527, https://doi.org/10.1016/j.inoche.2022.109527.

[43] Mohammad Alizadeh, M.; Salimi, F.; Ebrahimzadeh-Rajaei, G., Sensing of Sarin Nerve Agent by BN Nanoclusters: DFT and TDDFT Calculation. *Braz. J. Phys.* **2022**, *52*(2), 56, https://doi.org/10.1007/s13538-022-01073-z.

[44] Suhta, A.; Saral, S.; Çoruh, U.; Karakuş, S.; Vazquez-Lopez, E., Synthesis, Single Crystal X-ray, Hirshfeld Surface Analysis and DFT Calculation Based NBO, HOMO–LUMO, MEP, ECT and Molecular Docking Analysis of N′-[(2,6-Dichlorophenyl) Methylidene]-2-{[3-(Trifluoromethyl) Phenyl] Amino} Benzohydrazide. *J. Struct. Chem.* **2024**, *65*(1), 196-215, https://doi.org/10.1134/S0022476624010189.

[45] Zhao, G.; Yan, W.; Wang, Z.; Kang, Y.; Ma, Z.; Gu, Z. G.; Li, Q. H.; Zhang, J., Predict the Polarizability and Order of Magnitude of Second Hyperpolarizability of Molecules by Machine Learning. *J. Phys. Chem. A* **2023**, *127*(29), 6109-6115, https://doi.org/10.1021/acs.jpca.2c08563.

[46] Gusarov, S., Advances in Computational Methods for Modeling Photocatalytic Reactions: A Review of Recent Developments. *Materials* **2024**, *17*(9), 2119, DOI: 10.3390/ma17092119.

[47] Carmona-Espíndola, J.; Flores, A.; Ireta, J.; Gázquez, J. L., Charge-Transfer Energy Through the Dipole Moment. *J. Chem. Phys.* **2024**, *161*(23), 234109, https://doi.org/10.1063/5.0235534.

[48] Ebrahimzadeh-Rajaei, G., Removal of Reactive Red-P2B from Aqueous Solutions by Montmorillonite Clay; Kinetics, Thermodynamic and Isotherm Studies. *Inorg. Chem. Commun.* **2023**, *149*, 110386, https://doi.org/10.1016/j.inoche.2022.110386.

[49] Nourzadeh, Z.; Anarjan, N.; Ebrahimzadeh Rajaei, G.; Jafarizadeh-Malmiri, H., Preparation and Characterization of Vitamin D Microemulsions Using Two-Component Surface-Active Stabilizer System. *Z. Phys. Chem.* **2022**, *236*(2), 257-274, https://doi.org/10.1515/zpc-2020-1630.

[50] Rezaei-Aghdam, E.; Shamel, A.; Khodadadi-Moghaddam, M.; Ebrahimzadeh Rajaei, G.; Mohajeri, S., Synthesis of TiO_2 and ZnO Nanoparticles and CTAB-Stabilized Fe_3O_4 Nanocomposite: Kinetics and Thermodynamics of Adsorption. *Res. Chem . Intermed.* **2021**, *47*, 1759-1774, https://doi.org/10.1007/s11164-020-04363-w.

[51] Rathika, A.; Reeda, V. J.; Divya, P., Synthesis, Spectroscopic Analysis (FT-IR, FT-Raman, UV, NMR), Non-Covalent Interactions (RDG, IGM) and Dynamic Simulation on Bis (8-Hydroxy Quinoline) Salicylate Salicylic Acid. *J. Mol. Struct.* **2024**, *1310*, 138231, https://doi.org/10.1016/j.molstruc.2024.138231.

[52] Rezvan, V. H.; Salehzadeh, J., Exploring Charge Transfer Complexes of Fluoroquinolone Drugs and π-Acceptors (Picric Acid and 3,5-Dinitrobenzoic Acid): DFT Insights Into Electronic Interactions, Thermodynamic Stability, FMOs, and NLO Properties. *ChemistrySelect* **2025**, *10*(15), e202405137, https://doi.org/10.1002/slct.202405137.